

First-Principles Design of Halide-Reduced Electrides: Magnetism and Topological Phases

Tonghua Yu,¹ Motoaki Hirayama,^{1,2} José A. Flores-Livas,^{2,3} Takuya Nomoto,¹ and Ryotaro Arita^{1,2}

¹*Department of Applied Physics, University of Tokyo, Tokyo 113-8656, Japan*

²*RIKEN Center for Emergent Matter Science, 2-1 Hirosawa, Wako, 351-0198, Japan*

³*Dipartimento di Fisica, Università di Roma La Sapienza, Piazzale Aldo Moro 5, I-00185 Roma, Italy*

We propose a design scheme for seeking potential electrides derived from conventional materials. Starting with rare-earth element based halides, we exclude the halogen and perform global structure optimization to obtain stable phases but having an excess of electrons confined inside interstitial cavities. Then, spin-polarized interstitial states are realized by chemical substitution with magnetic lanthanides. Interestingly, the band-topology analysis for the predicted systems evidences the possible emergence of topological magnetism in these electrides. We report two families of designed electrides, A_2C_2 and A_2Ge ($A = Y$ or Gd), both of which turn out to be topological nodal line semimetals (metals) in the absence of spin-orbit coupling and manifest spin-polarized interstitial states with the inclusion of Gd . Our work establishes an alternative computational approach of functional electrides design and highlights the magnetism and topological phases embedded in electrides.

I. INTRODUCTION

Electrides are a novel class of crystals with vacant cavities accommodating intrinsic excess electrons, which are not tightly constrained by certain nuclei, but on the contrary, form ionic bonds with the cationic framework, playing the role of anions^{1,2}. Different from the random defects or color centers, sites of interstitial electrons in electrides conform to the translational periodicity. Since the experimental synthesis of the first room-temperature stable inorganic electride $[Ca_{24}Al_{28}O_{64}]^{4+}(4e^-)$ ($C12A7:2e^-$)³, electrides have aroused great interests among the communities of materials science, chemistry and condensed matter physics, owing to the intriguing properties exhibited by non-nucleus-bound electrons. For instance, in magnetic electrides the spin-unpaired anionic electrons are well suited for spin injection in a spintronic device^{4,5}, on account of their low work function. In addition, the interstitial electronic states are found to favor band inversion near the Fermi level, giving rise to the high tendency for electrides towards topological phases^{6,7}. One could therefore implement electrides as an excellent testbed to study the topological physics⁸⁻¹².

The members of recognized electrides especially magnetic electrides, however, are extremely scarce¹³. Consecutive efforts have been devoted by a number of researchers to computational discovery of new electrides. Approaches of the mainstream involve: structure screening from the materials database^{7,14-16}, crystal structure prediction (CSP) for unknown prototype structures¹⁷, and functionality-tailored electrides design^{8,18}. Here we present an alternative computational strategy to design new electrides. It is widely noticed that every natural electride corresponds to a potential oxidized form, such as Ca_2N to Ca_2NCl , Y_2C to Y_2H_2C . One may ask if the reverse direction holds or not¹³. Namely, we pick a compound and remove the strong anion from it (e.g.,

remove Cl from Ca_2NCl), then the remaining structure, suspected to be a possible electride, is studied using a CSP method. We mainly focus on ternary halides containing rare-earth elements (i.e., Sc , Y , and lanthanides). A stable or metastable reduced form of those halides is expected to be candidates of binary electrides. Chemical substitution of magnetic lanthanides is followed to induce spin-polarized interstitial electronic states, by which magnetic electrides can be realized. Considering the intimate relationship between electrides and topological materials, we also study the electronic band topology upon the designed crystals, with the results showing that the majority of them belong to topological nodal line semimetals or metals (TNLSMs).

II. METHODS

A. Design scheme

The procedure of our design scheme is presented in Figure 1, starting from the selection of halides as electride hosts. Excess electrons as well as vacant space are two necessary conditions for electride formation⁷. Exclusion of the halogen gives rise to intrinsic excess electrons for the system. Meanwhile, we are exclusively interested in the crystals with large interstitial sites surrounded by cations after taking away halogens, where anionic electrons could reside. We restrict our scope to the known halides accessible from the Inorganic Crystal Structure Database (ICSD)¹⁹, with rare-earth elements (mainly La , Y , Sc) serving as cations. Because of low electronegativity and standard valence (usually $+3$), rare-earth elements are favorable electron donors in electrides. Additionally, close radii among rare-earth atoms are a good condition for chemical substitution (e.g. $Y \rightarrow Gd$). For concreteness, we choose 5 structure prototypes of initial halides, see Appendix A.

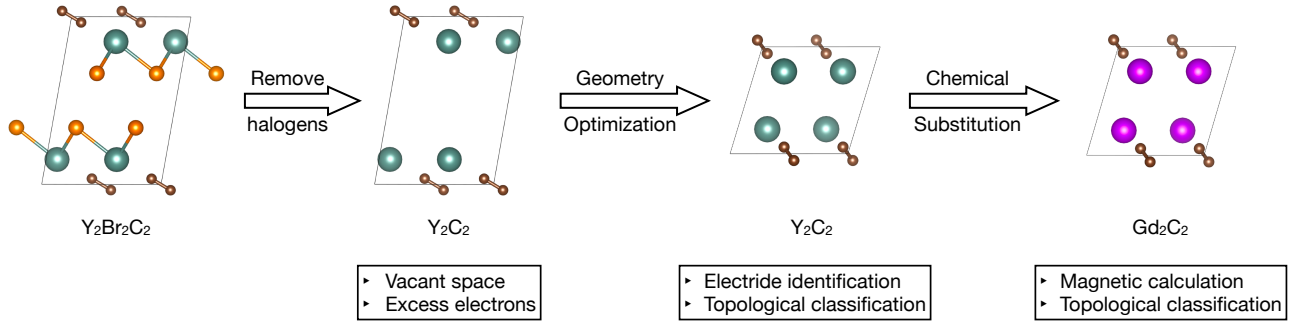


FIG. 1. Flowchart of designing halide-derived electrides. $\text{Y}_2\text{Br}_2\text{C}_2$ is taken as the example.

Simply removing atoms from a material may lead to a very unstable state. As a result, CSP necessarily follows to eliminate the instability. Stable and marginally stable states would be picked out for electride identification. From the viewpoint of CSP, the reduced structure of a known material works as a reasonable initial guess, assisting CSP to reach the ground state more efficiently, in contrast to random starting structures¹⁷. The La in lanthanum based compounds is replaced by Y in order to reduce the computational costs. Notice that although the size of interstitial regions might be compressed during CSP, proper vacant spaces adopting anionic electrons are often found among stable or marginally stable structures in practice.

Once the output materials of CSP are prepared, we determine if they are possible to be electrides or not, as stated in Sec. II B. Promising electrides are further examined for topological classification. At the same time, magnetic lanthanides (mainly Gd) would replace the original cations to introduce magnetism. Stability can not only be presumed by the similar atomic radii of substitution elements, but also be confirmed in accordance with the negative formation energy. Here, ferromagnetic (FM) configurations are particularly favored, in which anionic electrons easily become spin-unpaired. The ground magnetic configuration would be computationally claimed, estimating the relative stability of the FM state (see Sec. II B). Again, we analyze the topological nature of magnetic electrides.

B. Computational methods

All the electronic structure calculations are performed with the density-functional theory (DFT) based on the projector augmented wave scheme²⁰ as implemented in the Vienna *ab initio* simulation package (VASP)²¹. The exchange-correlation functional is given by the generalized gradient approximation (GGA) of the Perdew-Burke-Ernzerhof (PBE) type²². Strong intra-atomic interaction in lanthanide compounds are approximated by the GGA+U²³. The energy cutoff of the plane wave is chosen as 30% above of the maximal recommended value

in the pseudopotential library. The Brillouin zone is sampled by the Γ -centered grid with the resolution of $2\pi \times 0.03 \text{ \AA}^{-1}$. All atoms are fully relaxed with a force criterion of 0.002 eV/\AA . Pre/Post-processing tools and utilities for solids computation^{24–28} are employed.

Crystal structure searches for various compositions of electrides were performed with the minima hopping (MH)²⁹ algorithm with a generalized version to periodic systems employing variable cell shape molecular dynamics^{30,31}. This is a well-tested methodology that aims at finding the global minimum of complex condensed matter systems³². As aforementioned, we did not only consider the lowest energy configuration, but neighboring local minima were also considered for its potential as an electride. The formation of energy and dynamical stability was evaluated for the best candidates to verify its potential synthesis. To assess the lattice dynamics, we use the supercell approach, on which the total energy and pattern of displacements (within the harmonic approximation) were evaluated with VASP. The harmonic interatomic force constants were built and diagonalized using the ALAMODE software³³.

We utilize the cluster multipole (CMP) expansion approach^{34,35} to explore the possible stable magnetic states. The CMP is an orthogonal basis set of magnetic multipole configurations that could expand an arbitrary magnetic structure. By high-throughput benchmark, it turns out that the most stable magnetic configurations in nature are linear combinations of only few CMPs³⁶. For those electrides containing magnetic lanthanides, we therefore exploit DFT calculation to seek the stable configurations, with the initial magnetic moments generated by CMPs and their combinations. In the case that the FM state is a local minimum instead of a global one, the energy difference higher than the global minimum is employed to evaluate the energetic stability of the FM structure.

Crystalline symmetry eigenvalues of crossing bands along the high-symmetry line are preliminarily determined through *irvsp*, a software package that can obtain irreducible representations of the electronic Bloch states³⁷. Tight-binding models in Wannier representation³⁸ are constructed through Wannier func-

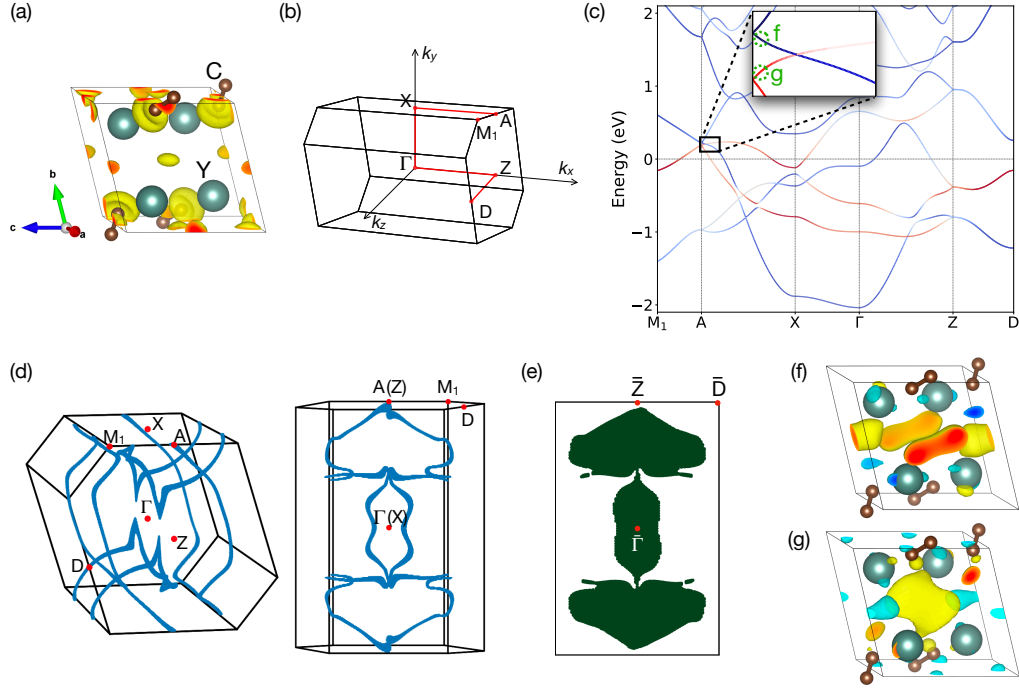


FIG. 2. Electronic properties from the bulk calculation of Y_2C_2 . (a) Primitive cell of Y_2C_2 . Yellow bubbles represent ELF. (b) The Brillouin zone of Y_2C_2 . The high-symmetry points and the path chosen is highlighted in red. (c) Projected band structure of Y_2C_2 along the path denoted in (b). The Fermi energy is set 0. As the color changes from red to blue, the contribution of interlayer states diminishes. The inset is a zoom-in view. (d) Nodal line of Y_2C_2 in the reciprocal space. The left and right panels are viewed from x and y directions respectively. Green and white separately stand for π and 0 values. High-symmetry points in this projected reciprocal space are also shown. (e) Zak phase integrated along y direction. (f)(g) Real branches of wavefunctions with the corresponding positions indicated in (c). The yellow and cyan mean positive and negative parts, respectively; red and blue stand for their cross-sections.

tions without the iterative maximal-localization procedure to preserve the symmetries of atomic orbitals^{39–42}. Considering the non-nucleus-bound electronic states are mostly s -like³, we set the s orbital as the trial projection at interstitial sites.

C. Electrides identification

Of all mature theoretical descriptors of electrides^{7,13,43,44}, electron localization function (ELF)^{45,46} is one of the reliable methods. Throughout our design, the appearance of ELF local maxima (irregardless of its magnitude⁷) at the vacant region would be the first step to recognize a potential electride. For the further identification, we do the fatband analysis, projecting eigenstates onto the s orbital of empty spheres (pseudoatoms) located at the vacancy positions with ELF maxima. On account of the large spread of non-nucleus-bound electrons, the pseudoatoms are set to cover a small portion of adjacent true atom regions defined by the Wigner-Seitz radii, so that the interstitial states could be captured as much as possible. Note that even in this way the contribution of anionic electrons might still be underestimated for some systems, espe-

cially for 2D electrides (see the discussion in Sec. III B). The wavefunction on the interstitial-state dominating bands as well as partial charge density close to the Fermi energy also provide additional proof.

III. RESULTS

A. Benchmark of the design scheme and overview of predicted electrides

Y_2C with the anti- CdCl_2 structure is a typical two-dimensional (2D) electride, experimentally confirmed and extensively studied⁴⁷. We apply our prediction method to three ternary chlorides that share similar structures with Y_2C , where Cl atoms occupy interlayer regions instead (see Appendix A). In the end, the expected electride state Y_2C as the global minimum is predicted by MH, demonstrating the repeatability of our design strategy.

Throughout the calculation, 5 types of structures (ex-

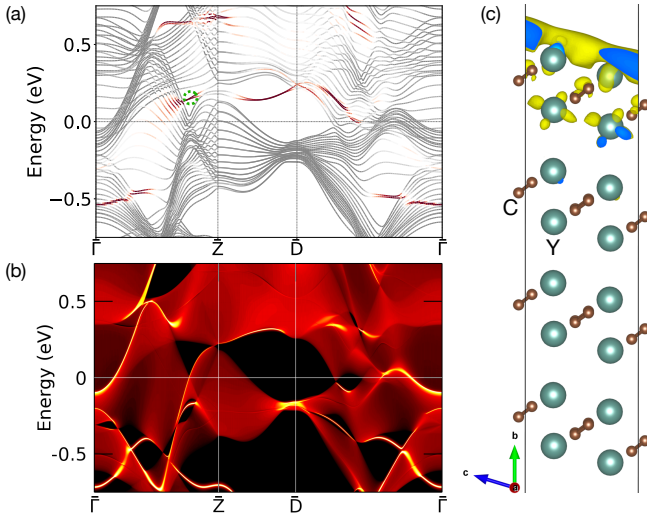


FIG. 3. Surface states of Y_2C_2 . (a) Electronic band structure of a Y_2C_2 slab along the b axis. High-symmetry points in the reduced Brillouin zone are given by Figure 2(e). Energy is measured from the Fermi level. The red indicates a large proportion of floating electronic states that localize on the slab's top and bottom. (b) Momentum-resolved surface density of states of the semi-infinite (010) slab. The same k -path with (a) is adopted. Yellow and dark red correspond to high and low density, respectively. (c) The squared wavefunction of a surface state localized around the top layer. The corresponding point in the momentum-energy space is marked in (a).

cluding the one for benchmark) are explored, each of which contains one to three halides, as presented in Figure 7 of Appendix A. Due to the variance of atomic distribution, different materials affiliated to the same structure category increase the variety of initial conditions for MH. Finally, we identify 3 new families of binary electrides, A_2C , A_2C_2 , and A_2Ge ($A = \text{Y}, \text{Gd}$), as given in Appendix A. In order to exemplify these new crystals, we shall focus on two of them (A_2C_2 and A_2Ge) as the representative examples in the subsequent discussion.

B. A_2C_2 system

Starting from $\text{Y}_2\text{Br}_2\text{C}_2$ ⁴⁸, we predict a metastable nonmagnetic crystal Y_2C_2 , with the formation energy -0.27 eV/atom, showing no imaginary branch (Appendix B). This is an original material, not recorded in the database¹⁹. Figure 2 (a) shows the primitive cell of Y_2C_2 , composed of four Y atoms and four C atoms. Unlike the well-known 2D electride Y_2C , carbons in Y_2C_2 become dimerized, playing less role near the Fermi level. Y_2C_2 shows a monoclinic structure with the principle axis along the a direction, having the space group $\text{P}2_1/\text{c}$ (No.14), which includes a inversion symmetry, a C_2 screw symmetry along a axis, and a glide symmetry in terms of a plane perpendicular to a axis. Indicated by ELF, Y_2C_2 is a promising 2D electride, where excess electrons

are distributed between cationic layers (Figure 2 (a)).

Since Y and C are both relatively light elements, we calculate the electronic band structure in the absence of spin-orbit coupling (SOC), along the high-symmetry path given by Figure 2(b). The number of valence electrons in this calculation is 60. Hence, the 30 lower bands are counted as valence bands (VBs), while the other higher bands are regarded as conduction bands (CBs). Contribution of anionic electrons is highlighted, by projecting eigenstates onto the s orbital of pseudoatoms placed at sites with local ELF maxima [i.e. (0, 0.5, 0) and (0.5, 0.5, 0.5)]. One can notice that interstitial states are closely related to bands around the Fermi energy E_F and show conducting behavior. In Figure 2 (f)(g), the real parts of two eigenstates affiliated to a highest VB and a lowest CB are depicted respectively, of which the corresponding positions in the band structure are marked in the inset of Figure 2(c), close to a gapless point. Non-nuclear orbitals are observed for both bands, further confirming the electride characteristics. Nevertheless, the downward band (from left to right), claimed by the projection analysis to have low portion of interstitial states, also contains non-nuclear orbitals according to the wavefunction. Such contradiction originates from the fact that those non-nuclear orbitals are just distributed in the uncovered region of pseudoatoms. The projection therefore underestimates the contribution from anionic electrons.

Next we move to the topic of band topology. The degenerate point between a VB and a CB, mentioned in the last paragraph, is located along the A - X line that has the C_2 symmetry. This degeneracy is protected by the opposite C_2 eigenvalues of the two crossing bands, indicated by `irvsp`. Such C_2 symmetry protection can also be concluded from the wavefunctions in Figure 2 (f)(g), although it is not straightforward⁴⁹. Due to the spatial inversion (\mathcal{P}) and time reversal (\mathcal{T}) symmetries in this spinless system^{50,51}, this degenerate point extends to general k -points and forms a snake-shape nodal line [Figure 2(d)]. In the manifold of the Brillouin zone, those disconnected nodal line segments should constitute a whole ring. It noteworthy that this nodal line partly comes from non-nucleus-bound electronic states (e.g. the band crossing in the A - X direction), which are insensitive to the relativistic effect of the nuclei field, therefore might exhibit a negligibly small gap even if SOC is present¹¹.

The nodal line here is protected by the π Berry phase, as one may confirm it by the computation of the Berry phase circling the line^{50,51}. Here we exploit a special version of Berry phase, known as the Zak phase, defined by

$$\gamma(\mathbf{k}_{\parallel}) = \sum_n^{\text{occ.}} \int_0^{|\mathbf{K}|} dk_{\perp} i \langle u_{n\mathbf{k}} | \nabla_{k_{\perp}} | u_{n\mathbf{k}} \rangle \quad (1)$$

for an arbitrary wave vector \mathbf{k} , where \mathbf{K} stands for the reciprocal lattice vector, k_{\perp} is the magnitude of \mathbf{k} component along \mathbf{K} and \mathbf{k}_{\parallel} is the other component perpendicular to \mathbf{K} ; $|u_{n\mathbf{k}}\rangle$ represents the cell-periodic Bloch function, with the gauge $|u_{n,\mathbf{k}+\mathbf{K}}\rangle = e^{-i\mathbf{K}\cdot\mathbf{r}}|u_{n\mathbf{k}}\rangle$. Making

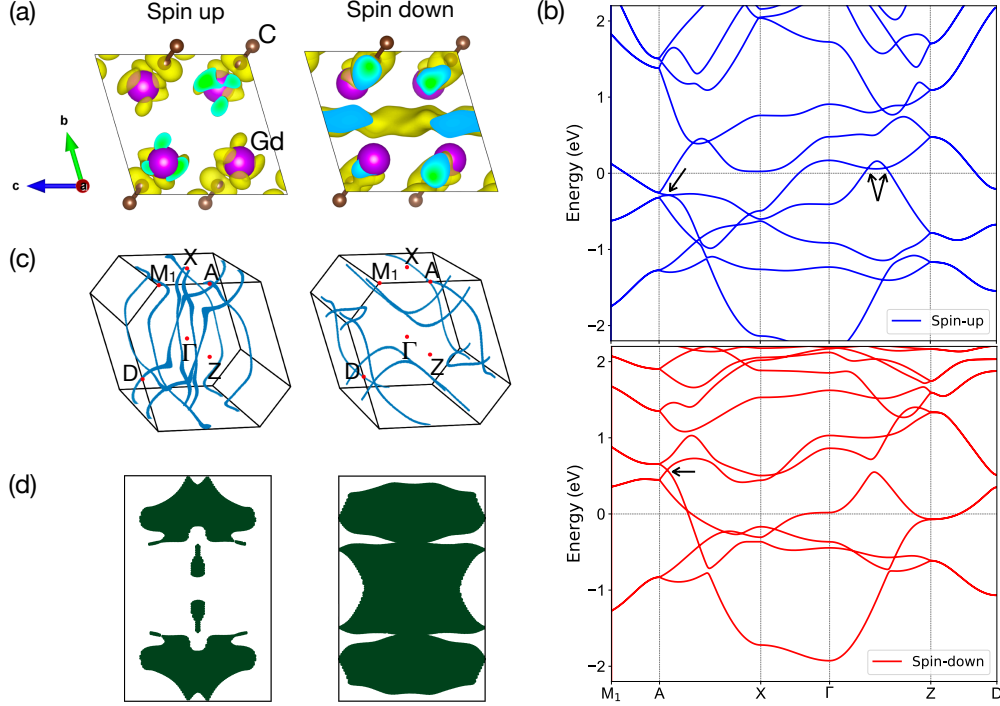


FIG. 4. Electronic properties of Gd_2C_2 . (a) Primitive cell of Gd_2C_2 . Partial charge density around the Fermi level ($-0.05 \sim 0.05$ eV) is shown for the spin-up (left) and spin-down (right). Yellow bubble represents the partial charge density, the green and blue are the cross sections. (b) Electronic band structure of FM Gd_2C_2 for the spin-up (top) and spin-down (bottom). The high-symmetry points are indicated in (c). (c) Nodal lines of FM Gd_2C_2 for the spin-up (left) and spin-down (right). Brillouin zone together with high-symmetry points are depicted too. (d) Zak phase for the spin-up (left) and spin-down (right), integrated along the y direction (i.e. Γ -X).

\mathbf{K} along y direction of the reciprocal space, yields the Zak phase distribution displayed in Figure 2(e), which is quantized to be 0 or π (mod 2π) as a result of \mathcal{PT} and $\text{SU}(2)$ symmetry. The nontriviality of this nodal line is demonstrated by the fact that the profile of π value region of the Zak phase just matches the nodal line projection along y direction [Figure 2(e) and the right panel of Figure 2(d)]. Y_2C_2 is therefore a TNLSM.

While showing the fingerprint of nodal lines in the bulk, the Zak phase also discloses information on the surface^{6,50,52}. At the wave vector \mathbf{k}_{\parallel} with π Zak phase, the bulk polarization is nonzero and quantized, and the topological charge $e/2$ (mod e) is induced at the surface by this bulk polarization. Using the DFT calculation upon a 15-layer (010) slab with the electron layer being cut, we get the electronic band structure as presented in Figure 3(a), whose high-symmetry points in the reduced Brillouin zone are given by the Figure 2(e). Contribution from excess electrons localized on the surfaces is highlighted by projecting eigenstates onto pseudoatoms on the top and bottom ends of the slab. Along the k -path segment where the Zak phase is quantized to be π , midgap states between the bulk VB and CB arise, although they are partially buried in the bulk spectrum (e.g. $\bar{\Gamma}$ - \bar{Z} line). We visualize a surface state distribution in real space as shown in 3(c). One prominent feature is

that the this boundary state is not tightly attached to any atoms, but floats on the surface instead. Such floating surface states are a hallmark of the topological electride model. Similar results were also revealed in other topological electrifieds like Y_2C_6 . Meanwhile, a tight-binding model is constructed based on the Wannier orbitals without maximal localization. The Bloch states are projected onto the Y $4d$ and interlayer s orbitals. Figure 3(b) depicts the momentum-resolved surface density of states (DOS) for a semi-infinite (010) slab by virtue of the iterative Green's function method and the tight-binding Hamiltonian. Interstitial s orbitals are located on the surface of the semi-infinite slab, modeling the floating anionic electrons. The DOS exhibits the same surface states as the slab bands do, in spite of slight difference caused by the boundary reconstruction during the DFT calculation. Both techniques unveil the emergence of in-gap states on the \bar{Z} - \bar{D} line, in which the Zak phase is 0 [Figure 2(e)]. Such surface states should be trivial and could be induced by the two floating Wannier orbitals on the slab surface⁵³. It is worth noting that these in-gap states are predicted to be absent by the tight-binding model if the Bloch states are projected onto the atomic orbitals only (see Appendix D). Therefore, we stress the essence of interstitial orbitals being projectors in Wannier representation, when researching the surface states

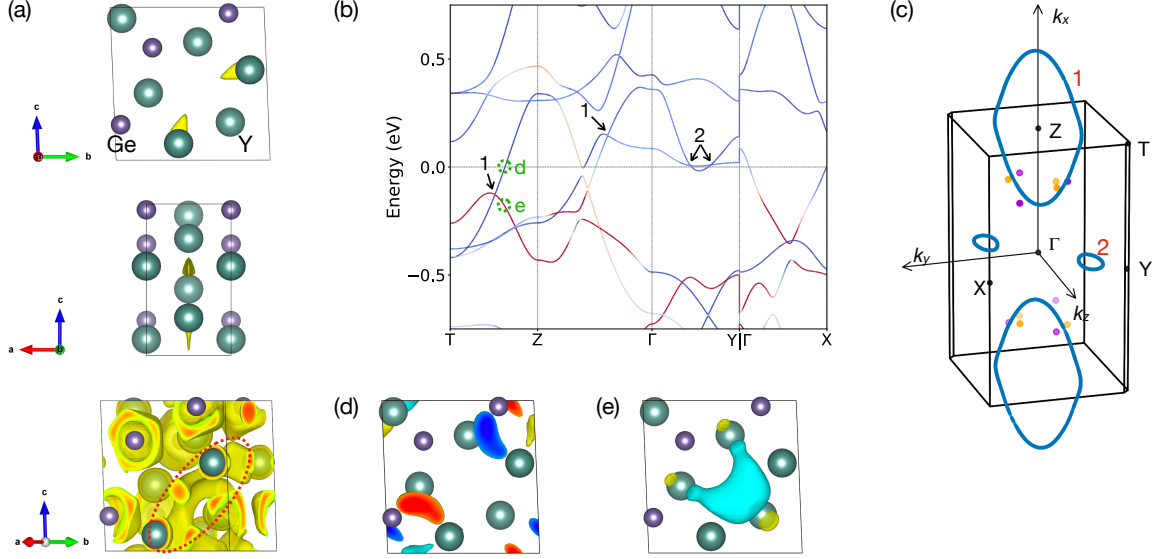


FIG. 5. Electronic properties from the bulk calculation of Y₂Ge. (a) The primitive cell of Y₂Ge. Yellow bubbles are ELF. The isosurface value in the bottom panel is smaller than that in the top and middle panels. Connected interstitial states are highlighted by a dashed red circle in the bottom panel. (b) Projected band structure of Y₂Ge with the high-symmetry points denoted in (c). The Fermi energy is set 0. As the color changes from red to blue, the contribution of interstitial states decays. Some gapless points are indicated by arrows. (c) Nodal lines of Y₂Ge accompanied by the Brillouin zone. Two inequivalent nodal lines are labels as 1 and 2, respectively. Spinless Weyl points are also displayed, with the orange and magenta representing the monopole charge +1 and -1 separately. (d)(e) show the real branch of the wavefunctions at the positions indicated in (b); the positive is in yellow and red the cross-sections; the cyan and blue are for the negative part.

of topological electrides (at least 2D electrides).

We now report the results of chemical substitution, from Y to Gd. After ionic relaxation, Gd₂C₂ is nearly isostructural to Y₂C₂. The FM Gd₂C₂ is a metastable state based on the prediction of the CMP expansion (see Appendix C). To account for the strong localization of 4*f* orbitals on Gd sites, Hubbard *U* has been included with $U - J = 6$ eV and $J = 0.7$ eV¹⁴; other values ($U - J = 3$ eV and 9 eV) are also checked, showing that only the dense flat 4*f* bands shift while other bands near the Fermi level remain unchanged. Figure 4(a) presents the partial charge density of the FM Gd₂C₂, in the vicinity of E_F ($-0.05 \sim 0.05$ eV) for two spin channels. While only intralayer electrons can be seen for the spin-up, excess electrons rest in the interlayer gap for the spin-down. Therefore, spin-polarized interstitial states are achieved in this FM system, although the macroscopic magnetism is dominated by Gd atoms. Figure 4(b) gives the electronic band structure of FM Gd₂C₂ without SOC. One can notice that bands of two spin channels resemble those in Y₂C₂, as a result of the close electronic configuration between Y and Gd, as well as the nearly identical crystal structure. Such a similarity was observed too in the electride system of Y₂C and Gd₂C^{14,54}. Therefore, we expect Gd₂C₂ exhibits a similar electronic behavior with Y₂C₂, especially regarding the band topology. Band degeneracy around the Fermi level are displayed in Figure 4(b). In parallel with Y₂C₂, these degenerate points turn out to extend in the reciprocal space, forming nodal rings

for both spin up and down [Figure 4(c)]. The nontriviality is again verified by the Zak phase (Figure 4(d)). In spite of the broken \mathcal{T} symmetry, the remaining \mathcal{P} symmetry still protects the π Berry phase nodal lines. This time reversal breaking TNLSM state was also reported in Gd₂C⁵⁴.

C. A₂Ge system

Y₂Ge is another predicted electride, derived from the La₂I₂Ge model⁵⁵. It is a newly designed material not found in the database¹⁹, with the structure stability supported by the negative formation energy -0.62 eV/atom, and the absence of imaginary phonon frequency (Appendix B). As a base-centered orthorhombic lattice, Y₂Ge has the space group *Amm*2 (No. 38). Figure 5(a) depicts the primitive cell of Y₂Ge that contains nine Y atoms and three Ge atoms. The crystalline symmetry elements are: a C_2 rotational axis [011], two mirror planes (011) and (100), perpendicular to each other. Notice that the inversion (\mathcal{P}) symmetry is absent. The spatial distribution of ELF is given in Figure 5(a). Two ELF maxima related by the mirror and C_2 rotational symmetry exist in the cationic cavities (the top and middle panels). These two interstitial sites are not isolated but connected with each other, which can be unveiled in the bottom panel with a smaller isosurface value of ELF. Now that these interstitial states are connected through the

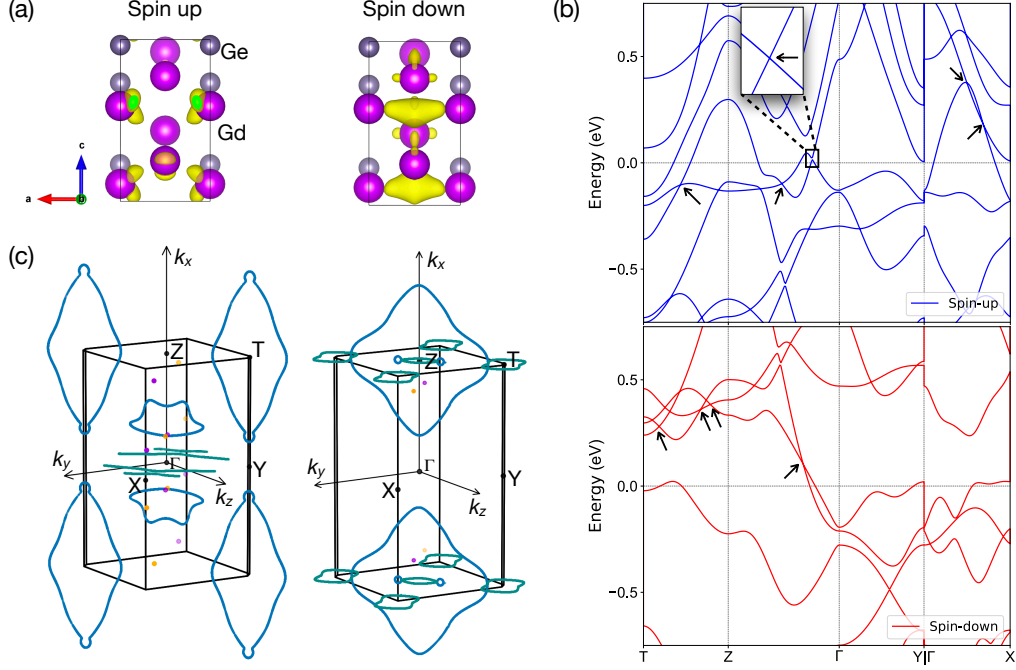


FIG. 6. Electronic properties of Gd₂Ge. (a) The primitive cell of Gd₂Ge. Partial charge density around the Fermi level ($-0.05 \sim 0.05$ eV) is presented for the spin-up (left) and spin-down (right). The yellow bubble represents the partial charge density, the green means the cross-section. (b) Electronic band structure of FM Gd₂C₂ for the spin-up (top) and spin-down (bottom). The high-symmetry points are indicated in (c). Degenerate points between the highest VB and lowest CB are marked by arrows. (c) Nodal lines of FM Gd₂C₂ for the spin-up (left) and spin-down (right). Brillouin zone, together with high-symmetry points, are depicted too. The blue or green distinguishes nodal lines that are distributed on the vertical or horizontal mirror plane. Weyl points are also displayed, with the orange and magenta representing the monopole and antimonopole, respectively.

one-dimensional (1D) channel, we classify this electrode candidate as 1D. Setting pseudoatoms at the interstitial locations with local maxima of ELF, yields the projected band structure of Y₂Ge (without SOC) given by Figure 5(b), in which the high-symmetry points are denoted in Figure 5(c). Eigenstates around the Fermi level mostly stem from Y 4d and interstitial *s* orbitals. Again the number of VBs is selected to match the half number of valence electrons in the primitive cell.

Along the T - Z - Γ - Y path, the gap between the highest VB and the lowest CB disappears at four positions, which have been labeled by arrows 1 or 2 in Figure 5(b). Since the T - Z - Γ - Y line is located on the mirror plane (011), each state on this line has a well-defined mirror eigenvalue (± 1 on account of the exclusion of SOC⁵¹), as verified by *irvsp*. It turns out that every pair of crossing bands have opposite mirror eigenvalues, protecting the degeneracy. In Figure 5(d)(e), two eigenstates – one is reflection antisymmetric and the other is symmetric with respect to the (011) plane – are particularly presented. Their corresponding positions have been indicated in Figure 5(b), belonging to a CB and a VB, respectively. Such opposite crystalline symmetries guarantee the band crossing in the T - Z direction. Moreover, one of the crossing bands is dominated by anionic electrons [Figure 5(e)], again suggesting the important role of

interstitial states for band inversion in electrides. Figure 5(c) reveals the nodal lines stemming from those gapless points are confined within the mirror plane (011). The big ring (labeled as 1) crosses the boundary of Brillouin zone; two small rings (labeled as 2) are the inversion of each other, associated by the \mathcal{T} symmetry. They are related to the band crossings indicated by the arrows 1 and 2 in Figure 5(b) respectively. We then implement the \mathbb{Z} -type reflection invariant to characterize the mirror-symmetry protected nodal lines^{51,56}. Within the mirror plane, we pick two points p_a and p_b on the two sides of the nodal line, at which the VBs and CBs are separated. Then count the number of VBs with the mirror eigenvalue $+1$, denoted by $N_{a,b}$. The reflection invariant reads

$$\zeta = N_a - N_b. \quad (2)$$

A nonzero ζ confirms the nontrivial nodal line, which means the band inversion cannot be adiabatically eliminated without breaking the mirror symmetry. In our case, one has $\zeta_1 = \zeta_2 = 1$ for the big and small nodal rings. As a result, the stability of the line nodes in Y₂Ge is protected by the reflection symmetry.

Aside from the line nodes, there appear six pairs of point nodes (spinless Weyl points) owing to the absence of \mathcal{P} symmetry. We compute the monopole charge (also

known as the chirality) of each node using the Berry flux across an enclosed surface accommodating the node⁵⁷. Figure 5(c) depicts the positions and monopole charges of the Weyl points. Each pair of Weyl points are linked by the \mathcal{T} symmetry, possessing the same monopole charge.

Next we replace the Y with Gd while retaining the crystal structure. While it is not highly energetic-stable in contrast to the magnetic ground state (Appendix C), the FM configuration is still allowable with the negative formation energy -0.97 eV/atom. Figure 6(a) displays the partial charge density distribution in the primitive cell, within the energy range -0.5 eV $< E - E_F < 0.5$ eV. Similar to Gd_2C_2 , interstitial states prefer the minority spin (spin down) in Gd_2Ge . That is, the magnetization opposite to Gd is induced among anionic electrons. Utilizing the GGA+U method, we show the electronic band structure in Figure 6(b) with SOC off. Compared to the bands of Y_2Ge , the spin-up bands are lowered and the spin-down are lifted as expected. Gapless points along high-symmetry lines are labeled by arrows. For the sake of brevity, we directly give the conclusion that these degenerated points are results of crossing bands which have opposite mirror eigenvalues just as Y_2Ge does. Besides, Figure 6(c) presents the nodal lines generated from the band crossings, lying in the mirror planes. Different from the Y_2Ge , $k_x = 0$ (spin up) and $k_x = \pi$ (spin up) planes also hold nodal lines (highlighted by green), which is a natural result of the mirror reflection with respect to the (100) plane in real space. Additionally, the perpendicular mirror planes give rise to two sets of nodal chains in the reciprocal space of spin-down. In parallel with Y_2Ge , Weyl points are observed for both spin channels (Figure 6(c)). The intriguing properties arose out of the coexistence of Weyl points and nodal chains remain to be explored⁵⁸.

IV. CONCLUSION

In summary, we proposed a new electride design scheme, predicting electrides as the reduced form of halides (i.e., removing the halogen). To demonstrate this design strategy, three new families of binary electrides, $A_2\text{C}$, $A_2\text{C}_2$, $A_2\text{Ge}$ ($A = \text{Y}, \text{Gd}$), derived from ternary halides are identified computationally, based on first-principles crystal structure prediction. These three families of electrides exhibit 3D, 2D, 1D geometry confinement, respectively (the 3D electrides $A_2\text{C}$ are briefly discussed in Appendix A). Gd is introduced by chemical substitution so that magnetism can be assessed. Hence, we studied the ferromagnetic case and a situation where the anionic electron can easily be magnetized. Following our computational results, these are suitable for spin injection. The topological phases investigated thoroughly show that all the designed electrides manifest topological nodal lines in the reciprocal space, further confirming the close relation between electrides and topological materials due to the interstitial states around the Fermi

level. Our strategy to designed magnetic and topological electrides systems can be easily generalized to other sets of materials. For example, one could expand the searching space to include hydrides, oxides, nitrides, etc. accessible through material databases. Finally, the replacement/substitution of other lanthanides in host systems is likely to open new avenues to synthesize magnetic electrides.

ACKNOWLEDGMENTS

The authors thank Marie-Therese Huebsch for useful discussion on magnetic crystal structures. J.A.F.L acknowledges computational resources provided by the Swiss National Supercomputing Center withing the project s970.

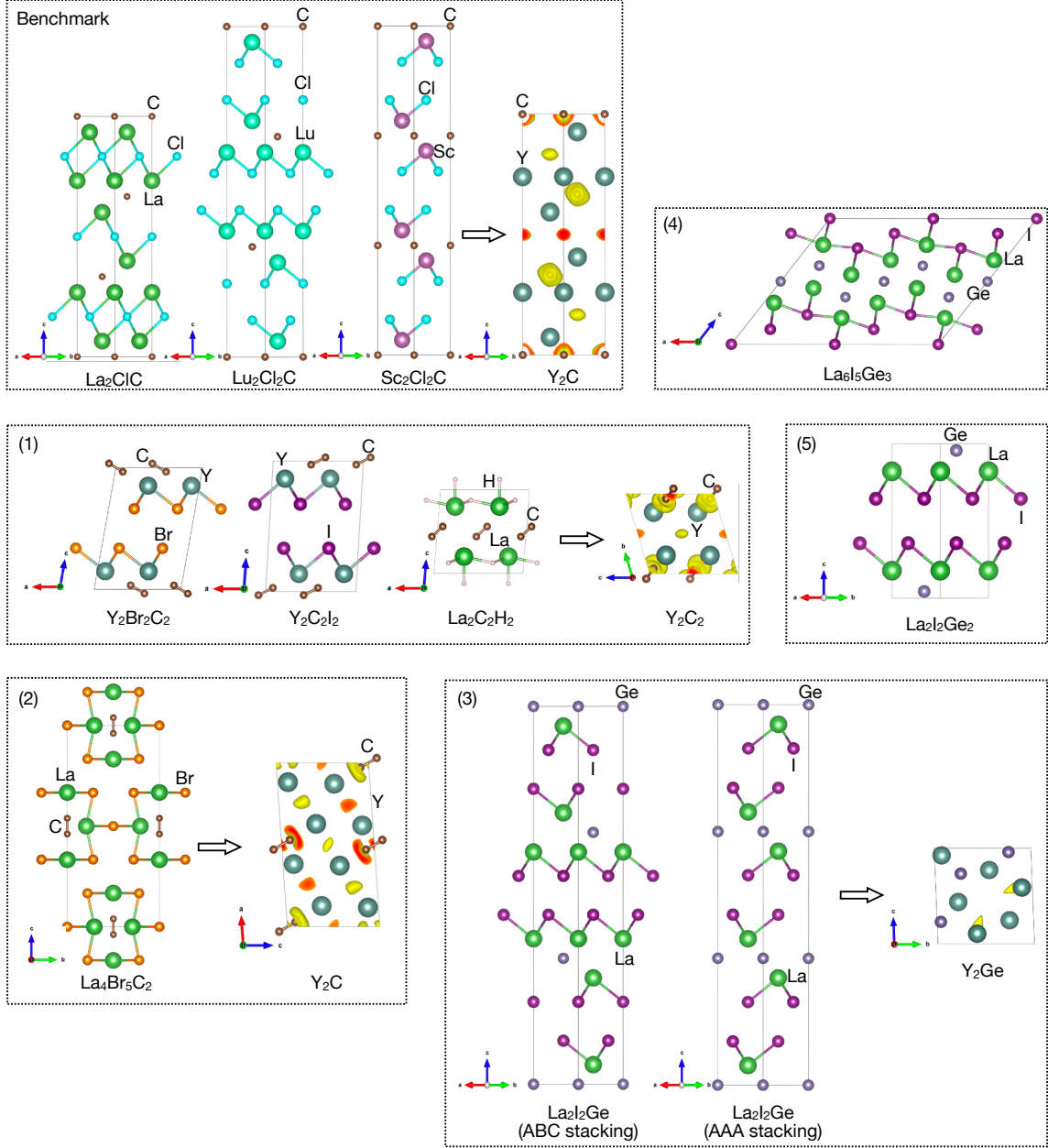


FIG. 7. Crystal structures of all the initial compounds and final possible electrides. Boxes classify the structure types. The evolution correspondence has been marked by black arrows. $\text{Sc}_2\text{Cl}_2\text{C}$, trigonal Y_2C (in the benchmark panel), monoclinic Y_2C [panel (2)], $\text{La}_2\text{I}_2\text{Ge}$ are displayed in the conventional unit cell (or supercell); others are primitive cells. Species of atoms have been labeled. ELF of electrides is represented by yellow bubbles.

Appendix A: Initial halides and designed electrides

In this Appendix we list the structures of initial ternary halides, as well as the final predicted electride candidates as stated in Sec. III A.

For benchmark three chlorides La_2ClC , $\text{Lu}_2\text{Cl}_2\text{C}$ and $\text{Sc}_2\text{Cl}_2\text{C}$ are selected, as shown in the first panel (right top) of Figure 7. Removing Cl and substituting Y for La, Lu or Sc, we have the ground state Y_2C after geometry optimization with MH in the end. Other 5 types of ini-

tial crystals (9 materials) are also presented in Figure 7, most of which are halides, with one exception $\text{La}_2\text{C}_2\text{H}_2$ (a hydride) that makes no difference with the exclusion of hydrogen.

Of the 5 classes of compounds, 3 classes [panels (1) ~ (3)] could evolve into binary electrides through our design procedure. Apart from Y_2C_2 and Y_2Ge that have been introduced in the main text, a polymorph of Y_2C with the monoclinic lattice (space group C2/m , No. 12) is a promising electride as well, whose conventional cell

and ELF are shown in the panel (2) of Figure 7. This structure is predicted to be the ground state derived from $\text{La}_4\text{Br}_5\text{C}_2$, despite that the energy is higher than the acknowledged 2D electride trigonal Y_2C (the firm C_2 dimer is almost impossible to be broken during the CSP, therefore the trigonal Y_2C with no dimerization cannot appear among the generated structures of $\text{La}_4\text{Br}_5\text{C}_2$). The monoclinic Y_2C exhibits 3D characteristics as those partially localized electrons (implied by the ELF maxima in the vacant space) in cavities are connected by delocalized electrons. Moreover, calculation suggests the existence of nodal lines protected by the π Berry phase. The ferromagnetic counterpart, Gd_2C , is predicted to be the ground configuration according to the CMP expansion.

Appendix B: Phonon spectra of Y_2C_2 and Y_2Ge

The phonon spectra of Y_2C_2 and Y_2Ge are shown in Figure 8. Both systems are dynamically stable, supporting further evidence towards their possible synthesis.

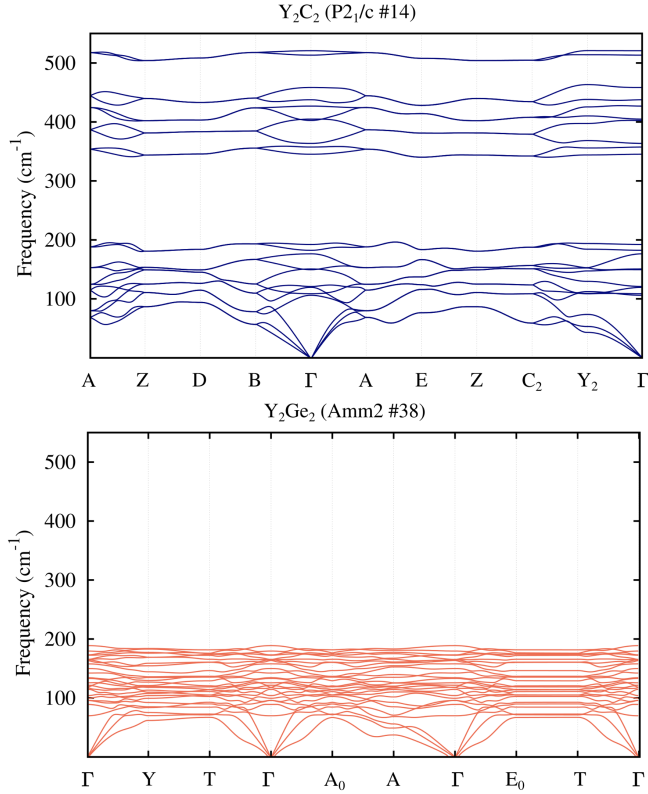


FIG. 8. Phonon spectra of Y_2C_2 and Y_2Ge respectively.

Appendix C: Ground magnetic states of Gd_2C_2 and Gd_2Ge

The ground magnetic configuration of Gd atoms is antiferromagnetic (AFM) for both, Gd_2C_2 and Gd_2Ge , as given in Figure 9. The total energy of AFM Gd_2C_2 is 0.32 meV (or 37 K) lower than that of the FM case, and energy difference is 41.3 meV (479 K) for the Gd_2Ge system.

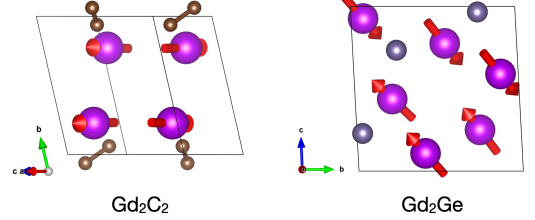


FIG. 9. Magnetic ground states of Gd_2C_2 and Gd_2Ge respectively. The red arrow stands for the direction of each spin.

Appendix D: Surface Density of States of Y_2C_2

In the same way of Sec. IIIB, we formulate the Wannier representation of Y_2C_2 here, but let the Y 4d and 5s orbitals (without the interstitial s) be the eigenstate projectors. The iterative maximal localization is not involved. Despite the matching between interpolated bulk bands and DFT bands, the ingap states along the \bar{Z} - \bar{D} line completely vanish according to the surface DOS [Figure 10].

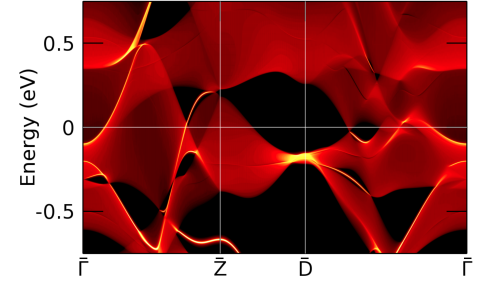


FIG. 10. Momentum-resolved surface DOS of a semi-infinite (010) slab of Y_2C_2 . All Wannier orbitals are located at atomic sites.

¹ J. L. Dye, Science **247**, 663 (1990).
² J. L. Dye, Science **301**, 607 (2003).
³ S. Matsuishi, Y. Toda, M. Miyakawa, K. Hayashi, T. Kamiya, M. Hirano, I. Tanaka, and H. Hosono, Sci-

ence **301**, 626 (2003).
⁴ X. Sui, J. Wang, and W. Duan, The Journal of Physical Chemistry C **123**, 5003 (2019).

- ⁵ S. A. Wolf, D. D. Awschalom, R. A. Buhrman, J. M. Daughton, S. von Molnár, M. L. Roukes, A. Y. Chtchelkanova, and D. M. Treger, *Science* **294**, 1488 (2001).
- ⁶ M. Hirayama, S. Matsuishi, H. Hosono, and S. Murakami, *Phys. Rev. X* **8**, 031067 (2018).
- ⁷ Q. Zhu, T. Frolov, and K. Choudhary, *Matter* **1**, 1293 (2019).
- ⁸ C. Park, S. W. Kim, and M. Yoon, *Phys. Rev. Lett.* **120**, 026401 (2018).
- ⁹ H. Huang, K.-H. Jin, S. Zhang, and F. Liu, *Nano Letters* **18**, 1972 (2018).
- ¹⁰ J. Wang, X. Sui, S. Gao, W. Duan, F. Liu, and B. Huang, *Phys. Rev. Lett.* **123**, 206402 (2019).
- ¹¹ X. Zhang, B. Fu, L. Jin, X. Dai, G. Liu, and Y. Yao, *The Journal of Physical Chemistry C* **123**, 25871 (2019).
- ¹² S. Nie, B. A. Bernevig, and Z. Wang, arXiv:2006.12502 (2020).
- ¹³ C. Liu, S. A. Nikolaev, W. Ren, and L. A. Burton, *J. Mater. Chem. C* **8**, 10551 (2020).
- ¹⁴ T. Inoshita, S. Jeong, N. Hamada, and H. Hosono, *Phys. Rev. X* **4**, 031023 (2014).
- ¹⁵ T. Tada, S. Takemoto, S. Matsuishi, and H. Hosono, *Inorganic Chemistry* **53**, 10347 (2014).
- ¹⁶ L. A. Burton, F. Ricci, W. Chen, G.-M. Rignanese, and G. Hautier, *Chemistry of Materials* **30**, 7521 (2018).
- ¹⁷ Y. Zhang, H. Wang, Y. Wang, L. Zhang, and Y. Ma, *Phys. Rev. X* **7**, 011017 (2017).
- ¹⁸ S.-C. Zhu, L. Wang, J.-Y. Qu, J.-J. Wang, T. Frolov, X.-Q. Chen, and Q. Zhu, *Phys. Rev. Materials* **3**, 024205 (2019).
- ¹⁹ G. Bergerhoff, R. Hundt, R. Sievers, and I. D. Brown, *Journal of Chemical Information and Computer Sciences* **23**, 66 (1983).
- ²⁰ G. Kresse and D. Joubert, *Phys. Rev. B* **59**, 1758 (1999).
- ²¹ G. Kresse and J. Furthmüller, *Phys. Rev. B* **54**, 11169 (1996).
- ²² J. P. Perdew, K. Burke, and M. Ernzerhof, *Phys. Rev. Lett.* **77**, 3865 (1996).
- ²³ A. I. Liechtenstein, V. I. Anisimov, and J. Zaanen, *Phys. Rev. B* **52**, R5467 (1995).
- ²⁴ V. Wang, N. Xu, J. Liu, G. Tang, and W. Geng, arXiv:1908.08269 (2019).
- ²⁵ U. Herath, P. Tavazde, X. He, E. Bousquet, S. Singh, F. Muñoz, and A. H. Romero, *Computer Physics Communications* **251**, 107080 (2020).
- ²⁶ W. Setyawan and S. Curtarolo, *Computational Materials Science* **49**, 299 (2010).
- ²⁷ A. Togo and I. Tanaka, arXiv:1808.01590 (2018).
- ²⁸ K. Momma and F. Izumi, *Journal of Applied Crystallography* **41**, 653 (2008).
- ²⁹ S. Goedecker, *The Journal of Chemical Physics* **120**, 9911 (2004).
- ³⁰ M. Amsler and S. Goedecker, *The Journal of Chemical Physics* **133**, 224104 (2010).
- ³¹ J. A. Flores-Livas, *Journal of Physics: Condensed Matter* **32**, 294002 (2020).
- ³² J. A. Flores-Livas, L. Boeri, A. Sanna, G. Profeta, R. Arita, and M. Eremets, *Physics Reports* **856**, 1 (2020).
- ³³ T. Tadano, Y. Gohda, and S. Tsuneyuki, *Journal of Physics: Condensed Matter* **26**, 225402 (2014).
- ³⁴ M.-T. Suzuki, T. Koretsune, M. Ochi, and R. Arita, *Phys. Rev. B* **95**, 094406 (2017).
- ³⁵ M.-T. Suzuki, T. Nomoto, R. Arita, Y. Yanagi, S. Hayami, and H. Kusunose, *Phys. Rev. B* **99**, 174407 (2019).
- ³⁶ M.-T. Huebsch, T. Nomoto, M.-T. Suzuki, and R. Arita, arXiv:2008.13669 (2020).
- ³⁷ J. Gao, Q. Wu, C. Persson, and Z. Wang, arXiv:2002.04032 (2020).
- ³⁸ Q. Wu, S. Zhang, H.-F. Song, M. Troyer, and A. A. Soluyanov, *Computer Physics Communications* **224**, 405 (2018).
- ³⁹ N. Marzari and D. Vanderbilt, *Phys. Rev. B* **56**, 12847 (1997).
- ⁴⁰ I. Souza, N. Marzari, and D. Vanderbilt, *Phys. Rev. B* **65**, 035109 (2001).
- ⁴¹ N. Marzari, A. A. Mostofi, J. R. Yates, I. Souza, and D. Vanderbilt, *Rev. Mod. Phys.* **84**, 1419 (2012).
- ⁴² G. Pizzi, V. Vitale, R. Arita, S. Blügel, F. Freimuth, G. Géranton, M. Gibertini, D. Gresch, C. Johnson, T. Koretsune, J. Ibañez-Azpiroz, H. Lee, J.-M. Lihm, D. Marchand, A. Marrazzo, Y. Mokrousov, J. I. Mustafa, Y. Nohara, Y. Nomura, L. Paulatto, S. Poncé, T. Ponweiser, J. Qiao, F. Thöle, S. S. Tsirkin, M. Wierzbowska, N. Marzari, D. Vanderbilt, I. Souza, A. A. Mostofi, and J. R. Yates, *Journal of Physics: Condensed Matter* **32**, 165902 (2020).
- ⁴³ S. Zhao, E. Kan, and Z. Li, *WIREs Computational Molecular Science* **6**, 430 (2016).
- ⁴⁴ S. G. Dale and E. R. Johnson, *The Journal of Physical Chemistry A* **122**, 9371 (2018).
- ⁴⁵ A. D. Becke and K. E. Edgecombe, *The Journal of Chemical Physics* **92**, 5397 (1990).
- ⁴⁶ A. Savin, *Journal of Molecular Structure: THEOCHEM* **727**, 127 (2005).
- ⁴⁷ X. Zhang, Z. Xiao, H. Lei, Y. Toda, S. Matsuishi, T. Kamiya, S. Ueda, and H. Hosono, *Chemistry of Materials* **26**, 6638 (2014).
- ⁴⁸ A. Simon, M. Bäcker, R. Henn, C. Felser, R. Kremer, H. Mattausch, and A. Yoshiasa, *Zeitschrift für anorganische und allgemeine Chemie* **622**, 123 (1996).
- ⁴⁹ The eigenvalue of C_2 rotation is complex in general. Therefore, a sole real part or imaginary part of the eigenwavefunction would not mimic itself after (screw) rotation. This is different from the case of reflection symmetry in spinless systems (Sec. III C).
- ⁵⁰ Y.-H. Chan, C.-K. Chiu, M. Y. Chou, and A. P. Schnyder, *Phys. Rev. B* **93**, 205132 (2016).
- ⁵¹ C. Fang, H. Weng, X. Dai, and Z. Fang, *Chinese Physics B* **25**, 117106 (2016).
- ⁵² D. Vanderbilt and R. D. King-Smith, *Phys. Rev. B* **48**, 4442 (1993).
- ⁵³ Each Wannier orbital on the surface contributes $e/2$ polarization charge (π Zak phase in the bulk) for certain areas \mathbf{k}_{\parallel} in the 2D reciprocal space. Then in the common area the total Zak phase is 0 (mod 2π) for that \mathbf{k}_{\parallel} . The surface states generated by these two floating orbitals, however, would not vanish, explaining the existence of in-gap bands even if the Zak phase is 0.
- ⁵⁴ S. Liu, C. Wang, L. Liu, J.-H. Choi, H.-J. Kim, Y. Jia, C. H. Park, and J.-H. Cho, arXiv:2007.05695 (2020).
- ⁵⁵ H. Mattausch, C. Zheng, M. Ryazanov, and A. Simon, *Zeitschrift für anorganische und allgemeine Chemie* **631**, 302 (2005).
- ⁵⁶ C.-K. Chiu and A. P. Schnyder, *Phys. Rev. B* **90**, 205136 (2014).
- ⁵⁷ M. Hirayama, R. Okugawa, and S. Murakami, *Journal of the Physical Society of Japan* **87**, 041002 (2018).

⁵⁸ J.-P. Sun, D. Zhang, and K. Chang, Phys. Rev. B **96**, 045121 (2017).